

# Optical Engineering

[SPIDigitalLibrary.org/oe](http://SPIDigitalLibrary.org/oe)

## **Measuring displacement fields by cross-correlation and a differential technique: experimental validation**

José Xavier  
António M. R. Sousa  
José J. L. Morais  
Vitor M. J. Filipe  
Mario Vaz



**SPIE**

# Measuring displacement fields by cross-correlation and a differential technique: experimental validation

**José Xavier**  
**António M. R. Sousa**  
**José J. L. Morais**  
CITAB/UTAD  
5001-801 Vila Real, Portugal  
E-mail: jmcx@utad.pt

**Vitor M. J. Filipe**  
CIDESD/UTAD  
5001-801 Vila Real, Portugal

**Mario Vaz**  
FEUP  
INEGI/LOME  
4200-465 Porto, Portugal

**Abstract.** A digital image correlation (DIC) algorithm for displacement measurements combining cross-correlation and a differential technique was validated through a set of experimental tests. These tests consisted of in-plane rigid-body translation and rotation tests, a tensile mechanical test, and a mode I fracture test. The fracture mechanical test, in particular, was intended to assess the accuracy of the method when dealing with discontinuous displacement fields, for which subset-based image correlation methods usually give unreliable results. The proposed algorithm was systematically compared with the Aramis® DIC-2D commercial code by processing the same set of images. When processing images from rigid-body and tensile tests (associated with continuous displacement fields), the two methods provided equivalent results. When processing images from the fracture mechanical test, however, the proposed method obtained a better qualitative description of the discontinuous displacements. Moreover, the proposed method gave a more reliable estimation of both crack length and crack opening displacement of the fractured specimen. © 2012 Society of Photo-Optical Instrumentation Engineers (SPIE). [DOI: 10.1117/1.OE.51.4.043602]

Subject terms: digital image correlation; optical flow; displacement fields.

Paper 111428 received Nov. 15, 2011; revised manuscript received Jan. 18, 2012; accepted for publication Feb. 3, 2012; published online Apr. 6, 2012.

## 1 Introduction

Several full-field optical techniques (FFOTs) for displacement and strain measurements have been proposed and developed.<sup>1</sup> Considering the physical phenomena involved in the measurements, they can be generically sorted into interferometric (e.g., speckle and moiré interferometry or shearography) and white-light (e.g., digital image correlation or grid and moiré methods) optical techniques. Interferometric techniques are based on the interference of light waves. These techniques have high sensitivity and accuracy but require specific and expensive experimental setups (e.g., lasers and antivibration tables). White-light techniques, on the other hand, are based on spatial variation of light intensity reflected from a target textured object. These techniques require simpler experimental setups (e.g., a camera-lens optical system) than their interferometry counterparts. FFOTs, although initially expensive, have been increasingly used in different engineering applications to take advantage of contact-free, full-field measurements over a spectrum of length scales.

Among FFOTs, digital image correlation (DIC) has become widely used, following the development of digital cameras and automatic digital image processing techniques.<sup>2,3</sup> This computer vision technique has the advantages of a simple principle and experimental setup that can switch from large down to small scales of observation (from structural down to micro- or nanoscales). It is based on digital image processing, in contrast with complex fringe analysis of interferometric techniques (phase evaluation and phase unwrapping methods). To enhance the accuracy of the DIC method, subpixel algorithms have been developed

to overcome the limitation of the pixel size unit.<sup>4,5</sup> The measuring errors obtained by DIC methods have also been investigated using both numerical<sup>6</sup> and experimental<sup>7</sup> validation tests.

In the classic DIC method, the domain of the image is first subdivided into subsets. A mathematical correlation is then performed between a pair of images that were taken before and after a given deformation of the target object, to estimate the displacement vector of the center of each subset. Therefore, one clear disadvantage of this technique is the spatial resolution, i.e., the smallest distance between two statistically independent measuring points. This issue can be a drawback, specifically in applications with discontinuous displacement fields (e.g., fracture mechanic studies) or when high strain gradients are present. To overcome this limitation, novel DIC algorithms have been proposed. Jin and Bruck<sup>8</sup> have proposed a genetic algorithm optimization coupled with digital image correlation to estimate the displacements at each pixel in a subset, keeping subpixel accuracy. The authors used both numerical and experimental tests for validation. This piecewise approach allows for fine spatial resolution but can be time-consuming and sensitive to convergence with regard to initial guess and domain of design variables entered in the genetic algorithm code. Réthoré et al.<sup>9,10</sup> have proposed the so-called extended digital image correlation (X-DIC). In this method, the domain of the image is discretized by finite elements, in an approach similar to the extended finite element method (X-FEM).<sup>11</sup> The displacements are then determined at the nodal positions by globally correlation between reference and deformed images. Because of the type of element shape functions employed, this method can identify fracture parameters (stress intensity factor) and crack length in problems of fracture mechanics. Chen et al.<sup>12</sup> have proposed a two-step X-DIC

algorithm allowing error minimization in computing discontinuous full-field displacements with large rigid-body translation components. The authors verified the reliability of the method experimentally through a set of rigid-body and mechanical tests. Poissant and Barthelat<sup>13</sup> have proposed an algorithm in which subsets are allowed to split into two new correlation regions when in the presence of discontinuity of the material. The authors verified the robustness of the method on a set of numerical and experimental fracture mechanical tests in both mode I and mode II. In practice, however, a limitation of this approach may be the size of the split subsets with regard to the average size of the speckle pattern, since the correlation factor strongly depends on the speckle pattern within the correlation domain.

The core of our proposed pointwise DIC method has already been validated on a set of numerical tests performed on synthetic speckled-pattern images.<sup>14,15</sup> In the present work, we emphasize accuracy and robustness of the method when processing images from experimental tests, in which measurements can be sensitive to several sources of error (e.g., out-of-plane movements, lighting, speckle pattern).<sup>7</sup> To start with, in-plane rigid-body translation and rotation tests were analyzed. Tensile mechanical tests were then performed on a resin epoxy material. Moreover, the accuracy of the method in processing discontinuous displacement fields was investigated. Single-edge notch/three-point bending (SEN-TPB) fracture test in mode I was carried out. Throughout this experimental validation, the proposed DIC method was systematically compared to GOM Aramis® DIC-2D 6.02 commercial software<sup>16</sup> by processing the same sequence of images.

## 2 Proposed DIC Method

The proposed digital image correlation method is divided into two main steps, which follow a coarse-fine approach: pixel-level (coarse) estimation and subpixel-level (fine) estimation of displacement fields. In the pixel-level step, the normalized cross-correlation is recursively applied over the sub-images obtained from the original images pair, using a quad-tree splitting process. On the subpixel-level step, an optical flow method based on a differential technique is used. An overview of the proposed method is presented in Fig. 1.

One of the constraints of optical flow is related to image intensity, which must be nearly linear across a given period of time.<sup>17</sup> The direct application of optical flow to calculate the displacement field on the surface of a specimen that undergoes a large deformation in a short period of time would introduce considerable errors in the resulting displacements.

Therefore, in our proposed method, a first step is introduced to calculate the pixel-level displacement of each sub-image. This procedure reduces to a minimum the pixel-level displacement of each pixel inside a sub-image (after being shifted), fulfilling the optical flow constraint. This enables optical flow technique to perform accurate measurement of subpixel displacement.

### 2.1 Pixel-Level Calculation

The pixel-level displacement estimation is performed over a pair of images obtained before (reference) and after (deformed) surface deformation. By use of a quad-tree image splitting process, each image is divided into a set of sub-images, and the normalized cross-correlation<sup>18,19</sup> is applied to obtain the displacement of each sub-image center point.

The image splitting (see Fig. 2) is similar to a quad-tree division process and is used to estimate pixel-level displacements between reference and deformed images, following a global-to-local approach. A global displacement is first calculated between full-sized images using the correlation coefficient. Next, both reference and deformed images are submitted to the splitting process using a quad-tree technique, which divides each image recursively into four sub-images and repeats for each pair the normalized cross-correlation. Once a predefined criterion<sup>14</sup> is fulfilled, this recursive procedure is stopped. As a final result of the splitting process, a coarse map is obtained of pixel-level displacements between the reference and deformed images.

### 2.2 Subpixel-Level Calculation

Once the pixel-level displacement between the two images is found, subpixel estimation is applied to obtain higher resolution. Each reference sub-image (resulting from the quad-tree decomposition) is shifted by its amount of pixel-level displacement over the corresponding deformed sub-image. Next, with a differential technique, the displacement of each pixel belonging to the sub-image is computed. The main stages of this processing consist of (1) prefiltering or smoothing with low-pass/band-pass filters (to extract signal structure of interest and enhance SNR); (2) extraction of basic measurements such as spatiotemporal derivatives (to measure the components of velocity); and (3) integration of the previously extracted measurements to produce a smooth 2-D flow field. In the proposed method, a 5- by 5-pixel Gaussian filter is first applied. Next, the derivatives are implemented using a local differential technique from

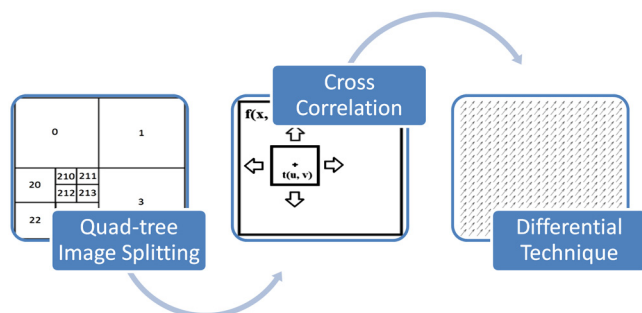


Fig. 1 Overview of the proposed method.

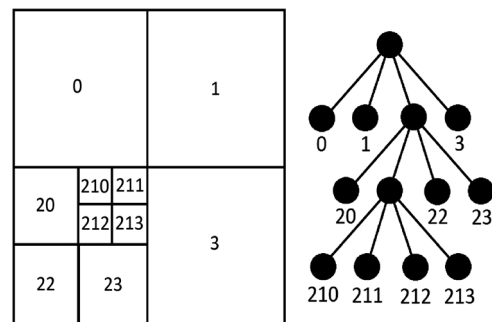


Fig. 2 Quad-tree image splitting process.

Lucas and Kanade.<sup>20</sup> Finally, the integration step is performed locally, through a least-squares calculation of the normal components of velocity, using an adequate window size (depending on the speckle size) designated by integration window (Table 1).

The resulting displacement field from applying this differential technique has subpixel resolution, usually with values less than 1 pixel. A pixel positioned at  $(x, y)$  with intensity  $I(x, y, t)$  in time instant  $t$  will have moved by  $\delta x, \delta y$  in time  $\delta t$ . Therefore, the following image constraint equation can be given:

$$I(x, y, z) = I(x + \delta x, y + \delta y, t + \delta t). \quad (1)$$

This assumption is true assuming that the movement between the two frames is relatively small. In this case, the image constraint at  $I(x, y, t)$  can be expressed with the Taylor series,

$$I(x + \delta x, y + \delta y, t + \delta t) = I(x, y, t) + \frac{\delta I}{\delta x} \delta x + \frac{\delta I}{\delta y} \delta y + \frac{\delta I}{\delta t} \delta t + \text{H.O.T.}, \quad (2)$$

where H.O.T. are the higher-order terms, which are assumed to be small enough to be ignored. From Eqs. (1) and (2) can be obtained

$$\frac{\partial I}{\partial x} \delta x + \frac{\partial I}{\partial y} \delta y + \frac{\partial I}{\partial t} \delta t = 0 \quad \text{or} \quad \frac{\partial I}{\partial x} \frac{\delta x}{\delta t} + \frac{\partial I}{\partial y} \frac{\delta y}{\delta t} + \frac{\partial I}{\partial t} = 0, \quad (3)$$

which results in

$$\frac{\partial I}{\partial x} V_x + \frac{\partial I}{\partial y} V_y + \frac{\partial I}{\partial t} = 0, \quad (4)$$

where  $V_x, V_y$  are the  $x$  and  $y$  components of image velocity, also known as the optical flow of  $I(x, y, t)$ , and  $\frac{\partial I}{\partial x}, \frac{\partial I}{\partial y}$ , and  $\frac{\partial I}{\partial t}$  are intensity derivatives of the image at  $(x, y, t)$  in the corresponding directions. Representing  $I_x, I_y$ , and  $I_t$  as the partial derivatives (intensity derivatives) from Eq. (4), the following equation is obtained:

**Table 1** Optical system components and measurement parameters.

	Experimental tests			
	Translation	Rotation	Tensile	Fracture
CCD Cameras				
Model	Baumer Optronic FWX20 (8 bits, 1624 × 1236 pixels)			
Shutter time (ms)	5	5	40	5
frequency (Hz)	2.5	(applied rotation)	(applied load)	0.1
Lenses				
Model	Nikon AF Micro-Nikkor			
	$f = 200$ mm; 4D	$f = 60$ mm; 2.8D	$f = 200$ mm; 4D	$f = 200$ mm; 4D
Aperture	$f/11$	$f/11$	$f/16$	$f/11$
Lighting				
	High Intensity LED Spotlight: CCS HSL-58SW-D300			
Working distance (mm) <sup>a</sup>	830	300	830	880
Conversing factor (mm/pixel)	0.0045	0.0216	0.0092	0.0123
Aramis 2D				
Facet size (pixels)	21 × 21	15 × 15	15 × 15	15 × 15
Step size (pixels)	21 × 21	15 × 15	15 × 15	15 × 15
Measuring points (macro-pixels)	49 × 46	80 × 91	60 × 98	78 × 106
Proposed DIC				
Integration window size (pixels)	22 × 22	40 × 40	15 × 15	15 × 15
Region of interest (pixels)	945 × 878	781 × 707	816 × 1379	1035 × 1495

<sup>a</sup>Distance from the specimen to the camera.

$$I_x V_x + I_y V_y = -I_t \quad \text{or} \quad \begin{bmatrix} I_{x_1} & I_{y_1} \\ I_{x_2} & I_{y_2} \\ \vdots & \vdots \\ I_{x_n} & I_{y_n} \end{bmatrix} \begin{bmatrix} V_x \\ V_y \end{bmatrix} = - \begin{bmatrix} I_{t_1} \\ I_{t_2} \\ \vdots \\ I_{t_n} \end{bmatrix} \quad \text{or} \quad A \rightarrow v = -b, \quad (5)$$

where  $A$  is the spatial intensity gradient,  $\rightarrow v$  the image velocity or optical flow at pixel  $(x, y)$  at time  $t$ , and  $b$  the time intensity derivative. To solve the overdetermined system of equations (integration step), the least-squares method can be used:

$$A^T A \rightarrow v = A^T (-b) \quad \text{or} \quad \rightarrow v = (A^T A)^{-1} A^T (-b) \quad (6)$$

or

$$\begin{bmatrix} V_x \\ V_y \end{bmatrix} = \begin{bmatrix} \sum_{i=1}^n I_{x_i}^2 & \sum_{i=1}^n I_{x_i} I_{y_i} \\ \sum_{i=1}^n I_{x_i} I_{y_i} & \sum_{i=1}^n I_{y_i}^2 \end{bmatrix} \begin{bmatrix} -\sum_{i=1}^n I_{x_i} I_{t_i} \\ -\sum_{i=1}^n I_{y_i} I_{t_i} \end{bmatrix}. \quad (7)$$

From Eq. (7), it is concluded that the optical flow can be found by calculating the derivatives of the image along all dimensions  $(x, y, t)$ .

### 2.3 Full-Field Displacement Evaluation

The displacement magnitude of each pixel is then obtained by adding its coarse pixel-level displacement (cross-correlation) with its respective finer subpixel-level displacement (differential technique).

## 3 Validation Test Methods

In this work, we evaluated the accuracy and robustness of the proposed pointwise DIC method by carrying out several experimental tests (Fig. 3): (a) in-plane rigid-body

translation test; (b) in-plane rigid-body rotation test; (c) tensile mechanical test; and (d) SEN-TPB mode I fracture test.

### 3.1 In-Plane Rigid-Body Translation Test

To start with, an in-plane rigid-body translation test was proposed, consisting of applying a constant displacement field to a target speckle region [Fig. 3(a)]. Considering a displacement along the  $x$  axis of the image, the displacement field in this case is simply given by

$$U(x, y) = U_0, \quad (8)$$

where  $U_0$  is the displacement value.

### 3.2 In-Plane Rigid-Body Rotation Test

An in-plane rigid-body rotation was then considered as illustrated in Fig. 3(b). A given in-plane rotation ( $\theta$ ) generates displacement fields in both  $x$  and  $y$  directions of the image. The angle of rotation can be determined as a function of the partial derivatives of the two components of the displacement field by the following relationship (small rotation assumption):

$$\theta = \frac{1}{2} \left[ \frac{\partial U(x, y)}{\partial y} - \frac{\partial V(x, y)}{\partial x} \right]. \quad (9)$$

### 3.3 Tensile Mechanical Test

The accuracy of the proposed DIC method in processing displacement fields corresponding to homogeneous strain fields was investigated by performing a mechanical tensile test [Fig. 3(c)]. In this test, a stress-strain ( $\sigma_x - \epsilon_x$ ) curve is obtained, describing the tensile behavior of the material. The nominal stress is defined by  $\sigma_x = P/A$ , where  $P$  is the applied load and  $A$  is the initial cross-section of the

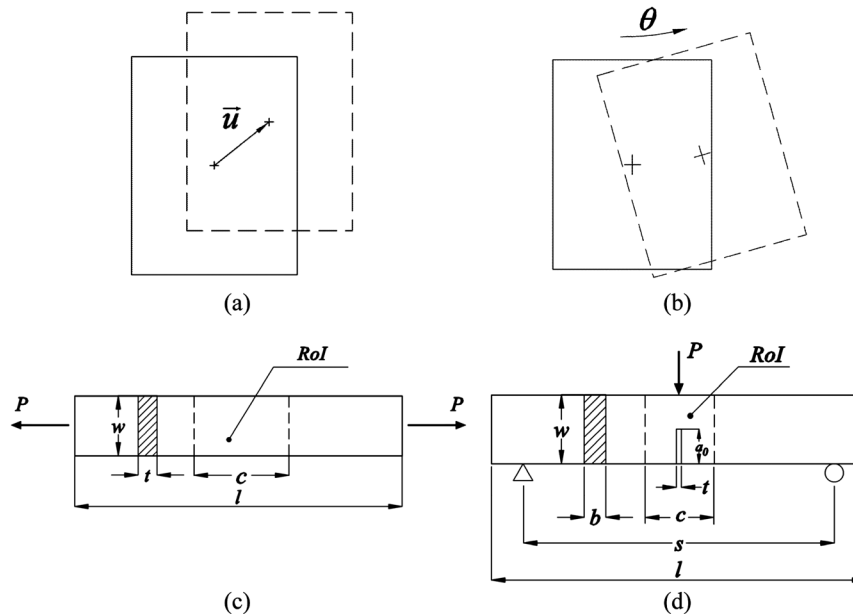


**Fig. 3** Experimental tests: (a) in-plane rigid-body translation test; (b) in-plane rigid-body rotation test; (c) tensile mechanical test ( $l = 180$ ,  $w = 10$ ,  $t = 2$ ,  $c = 13$ , RoI = region of interest); (d) single-edge notch/three-point bending (SEN-TPB) mode I fracture test ( $l = 120$ ,  $w = 20$ ,  $b = 2$ ,  $t = 3$ ,  $a_0 = 9.55$ ,  $s = 110$ ,  $c = 15$ , RoI = region of interest) (unit: mm).



specimen. The engineering strain is given as function of the displacement fields (assuming a linear elastic behavior with plane stress approach and small deformations) by

$$\varepsilon_{xx} = \frac{\partial U}{\partial x} = \frac{P}{EA} \quad \text{and} \quad \varepsilon_{yy} = \frac{\partial V}{\partial y} = -\frac{\nu P}{EA}, \quad (10)$$

where  $E$  and  $\nu$  are Young's modulus and Poisson's ratio, respectively.

### 3.4 Fracture Mechanical Test in Mode I

In studying fracture mechanics, three elementary crack propagation modes are considered: (a) opening mode or mode I; (b) sliding mode or mode II; and (c) tearing mode or mode III. In this work, we considered crack propagation in mode I.

In fracture tests, the raw data usually measured during crack propagation under stable and self-similar conditions are the applied load ( $P$ ), the displacement of its point of application ( $\delta$ ), the crack length ( $a$ ), and the crack opening displacement (COD).  $P$  and  $\delta$  can be measured directly by a universal testing machine. Among different techniques, displacement fields provided by DIC have been used for estimating crack length<sup>21–23</sup> and COD.<sup>24,25</sup> The use of DIC was found to be advantageous because of accuracy and relatively simple methodology.

#### 3.4.1 SEN-TPB test

Several tests can be used for evaluating fracture in mode I.<sup>26</sup> In this work, we chose the SEN-TPB test. The specimen and test configuration are schematically represented in Fig. 3(d). The specimen is a beam of length  $l$  and a cross-section of  $w \times b$ , with a machined notch of  $t \times a_0$  at its center. The beam rests on two supports with a span  $s$ , and the load  $P$  is applied in a three-point bending configuration. Fracture in mode I is assumed to occur along the extension ( $w - a_0$ ).

#### 3.4.2 Crack length

A method based on the variation of the distance among neighbor subsets has been proposed for estimation of the crack length.<sup>21–23</sup> The algorithm can be applied to a given set of four adjacent points, denoted by  $i, j, k$ , and  $l$  in the schematic representation of Fig. 4. An auxiliary function  $A$  is calculated based on the norm of the relative position vectors as

$$A(x, y) = \max(\|\mathbf{u}_i - \mathbf{u}_k\|; \|\mathbf{u}_j - \mathbf{u}_l\|), \quad (11)$$

where  $\mathbf{u}_p$  represents the displacement vector of point  $p$  (with  $p = i, j, k, l$ ). A criterion is then defined according to the following inequalities:

$$\begin{cases} M(x, y) = 1 & \text{if } A(x, y) \geq \alpha \bar{A} \\ M(x, y) = 0 & \text{if } A(x, y) < \alpha \bar{A} \\ M(x, y) = -1 & \text{if } A(x, y) = \text{No data} \end{cases}, \quad (12)$$

where  $\alpha$  is a constant value and  $\bar{A}$  represents the average of  $A(x, y)$ . The  $\alpha$  parameter works here as a threshold, in an approach similar to that of segmentation in digital image processing. This allows the definition of a mask  $M(x, y)$  [Eq. (12)] labeling the measuring region according to the following description:

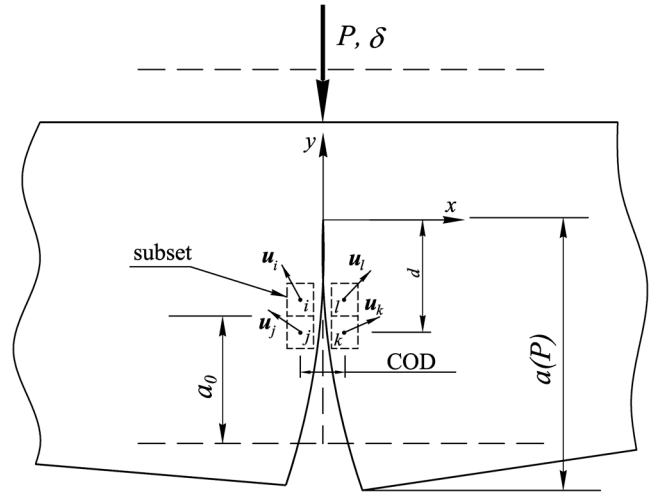


Fig. 4 Schema of crack propagation in mode I.

- $M(x, y) = 1$  defines the region where the material is damaged (assumed here around the crack tip);
- $M(x, y) = 0$  corresponds to regions where the material is undamaged;
- $M(x, y) = -1$  represents regions where no data are available because of crack propagation (boundary of discontinuity).

#### 3.4.3 Crack opening displacement

The COD is defined as the distance separating cracked surfaces, measured at a given distance behind the crack tip. The COD in mode I can be evaluated from the displacement field components provided by digital image correlation<sup>2</sup> as

$$\text{COD}_I = \|\mathbf{U}_j - \mathbf{U}_k\|, \quad (13)$$

where  $\mathbf{U}$  is the displacement field component perpendicular to the crack extension, associated with a pair  $(j, k)$  of correlation windows selected in opposite and symmetric parts with regard to the cracked surface (Fig. 4).

## 4 Experimental Work

### 4.1 Material and Speckle Pattern

The material used in this study was an SR 1500 epoxy supplied by Sicomin®, France, cured with SD 2503 hardener. Plates of  $200 \times 200 \times 2$  mm were cast in a mold from which the specimens were cut. The resin was cured at  $20^\circ\text{C}$  during 24 h, followed by 16 h at  $60^\circ\text{C}$ . According to the manufacturer, the expected Young's modulus of this resin is 2.860 GPa.

The region of interest of the specimens was painted to create a carrier speckle pattern suitable for digital image correlation. A white-based thin layer was first applied using an aerosol spray paint. A double-action airbrush was then used to achieve a random black-on-white pattern with suitable speckle size and contrast, as shown in Fig. 5.

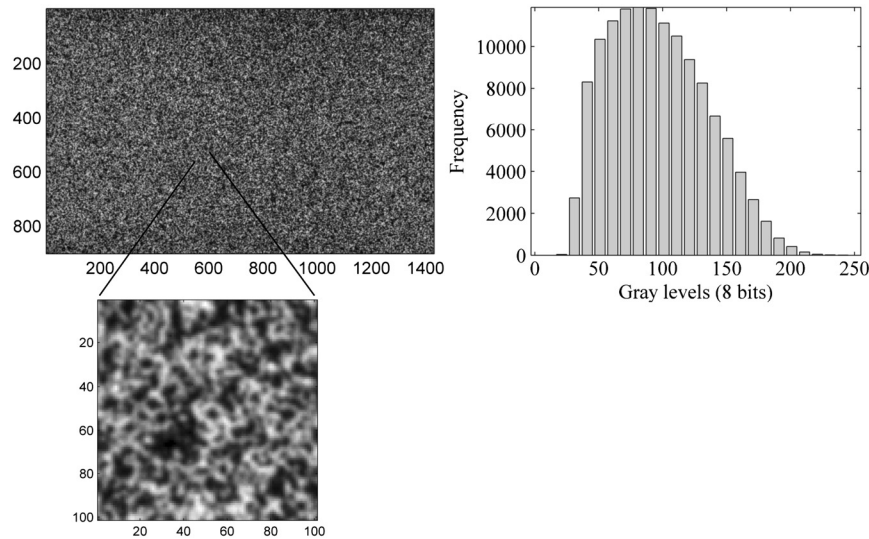


**Fig. 5** Speckled-pattern image and histogram (resolution:  $1431 \times 901$  pixels; region of interest:  $13.1 \times 8.2$  mm).

## 4.2 Test Methods: Experimental Setups

The components of the optical system used in the experimental setups are reported in Table 1. For the sake of comparison, the results obtained from the proposed method were discussed with respect to commercial GOM Aramis® DIC-2D 6.02 software,<sup>16</sup> when processing the same set of images. The measurement parameters of proposed and Aramis DIC methods are also summarized in Table 1.

### 4.2.1 In-plane rigid-body translation test

In the rigid-body translation test, the target specimen was mounted on the upper fixture of an Instron® 5848 MicroTester machine. Images of the sample free translation were acquired at a rate of 2.5 Hz, and the actuator displacement rate was set to 0.05 mm/min. Usually, this type of analysis is performed manually by means of a translation stage (e.g., Ref. 7), but for a more accurate evaluation of the reference displacement associated with each image, the translation test was performed here using a mechanical testing machine, under displacement control mode.

### 4.2.2 In-plane rigid-body rotation test

The rigid-body rotation test was performed manually using a metric goniometer NT55-841® (resolution of 0.1 deg). A sequence of images of the target specimen was recorded by imposing a rotation angle from 0.1 deg up to 0.5 deg with steps of approximately 0.1 deg.

### 4.2.3 Tensile mechanical test

In the tensile tests, rectangular coupons of epoxy polymer with nominal dimensions of  $l = 180$  mm,  $w = 10$  mm, and  $t = 2$  mm were tested [Fig. 3(c)]. The mechanical tests were carried out on an Instron 5848 MicroTester machine, at a displacement rate of 0.5 mm/min [Fig. 6(a)]. The applied load was measured by a load cell of 2 kN. Images were recorded with a frequency of 1 Hz (Table 1). A field of view at the center of the specimen covering an area of  $13 \times 10$  mm was imaged [Fig. 3(c)].

### 4.2.4 SEN-TPB test

A SEN-TPB specimen with nominal dimensions of  $l = 120$  mm,  $w = 20$  mm,  $b = 2$  mm,  $t = 3$  mm,  $a_0 = 9.55$  mm, and  $s = 110$  mm was used in the fracture tests [Fig. 3(d)]. A field of view of  $20 \times 15$  mm at the center of the specimen was imaged. The initial crack length was introduced in two steps. First, a notch (0.7 mm thick and 10 mm length) was machined with a circular saw and sharpened by indentation with a razor blade. The specimen was mounted on the actuator of an Instron 5848 MicroTester machine and displaced 0.25 mm at a rate of 100 mm/min. Before testing, the specimen was conditioned at 50°C and 84.6% relative humidity, until moisture saturation was attained. The equilibrium moisture content achieved under these hygrothermal conditions was 2.16%. Because of the plasticizing effect of absorbed moisture, the wet material exhibits a ductile fracture when tested at room temperature, with a stable crack growth. This feature enables the calculation of the crack length ( $a$ ) and the COD from the displacement field measured by digital image correlation. A complete fracture characterization of the epoxy material, however, was out of the scope of this work.

The SEN-TPB tests were performed in an Instron 5848 MicroTester machine with a controlled displacement rate of 0.2 mm/min [Fig. 6(b)]. The applied load was measured by a load cell of 2 kN. A sequence of images was recorded during the test with a frequency of 1 Hz (Table 1). A field of view at the center of the specimen covering an area of  $20 \times 15$  mm was imaged [Fig. 3(d)].

## 5 Results and Discussion

### 5.1 In-Plane Rigid-Body Translation Test

The displacement fields associated with each incremental rigid-body translation, with regard to a reference position, were measured by both the proposed and the Aramis DIC methods. As expected, a nearly constant displacement field was systematically measured across the entire region of interest. Thus, at each stage, the displacement was calculated as the mean value of the whole displacement field. The results comparing reference (applied) and calculated

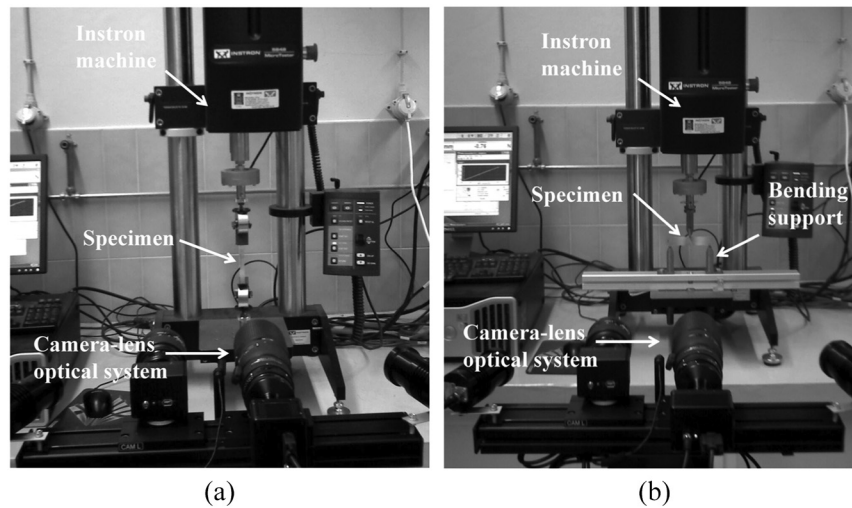


**Fig. 6** Photo-mechanical setup: (a) tensile test; (b) single-edge notch/three-point bending (SEN-TPB) fracture test.

displacements (mean and standard deviation) are shown in Fig. 7. The specimen underwent a total displacement of  $21.8 \mu\text{m}$  with increments of about  $2.4 \mu\text{m}$ . As can be seen, both methods followed accurately the reference-imposed displacements [Fig. 7(a)]. Moreover, a low scatter on the calculated displacement field at each stage was observed [Fig. 7(b)]. The proposed method had a lower standard deviation than the Aramis one, but more points were taken into account in the former (Table 1). These results validate the proposed method, according to the translation test performed.

### 5.2 In-Plane Rigid-Body Rotation Test

The set of images recorded in the rigid-body rotation test was processed to evaluate the displacement fields at each incremental rotation by the proposed and the Aramis DIC methods. At each stage, the applied rotation angle was estimated from the measured displacements according to Eq. (9). A polynomial least-squares approximation scheme was used for the numerical partial differentiation of the displacement components.<sup>27</sup> The order of the polynomial functions was chosen to be 3. The displacement field derivatives in

Eq. (9) were then calculated as the mean values over the whole region of interest. The mean and standard deviation associated with the calculated rotation angles are plotted with regard to the applied rotation in Fig. 8(a) and 8(b), respectively. It can be concluded that both proposed and Aramis methods are sensitive to the displacement fields generated by rigid-body rotations. Both methods approximately followed the imposed angles along the experiment. Some deviation from the reference values could be observed, however, especially at higher values of rotation; nevertheless, these values still had a low standard deviation [Fig. 8(b)]. This was also observed by other authors, who found the computed values for cross-correlation coefficients to be poorer as rotation angle increased.<sup>28</sup>

### 5.3 Tensile Mechanical Test

To process the data of the tensile mechanical tests, two images were taken at rest (reference configuration) and at a load of about 170 N (deformed configuration). An example of typical displacement fields measured by the proposed and Aramis DIC methods is shown in Fig. 9. As can be seen, the

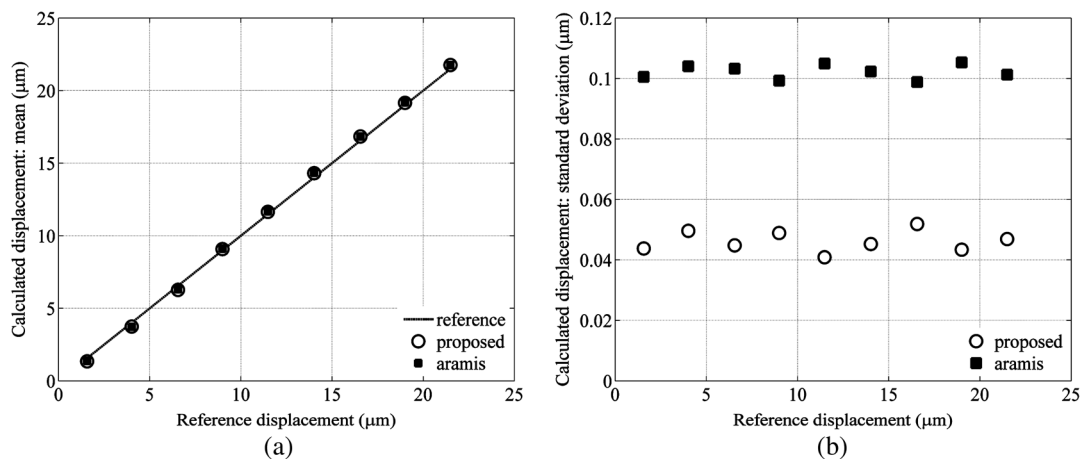


**Fig. 7** In-plane rigid-body translation test: mean (a) and standard deviation (b) of the calculated displacement field as a function of reference displacement obtained from proposed (○) and Aramis (■) digital image correlation methods.



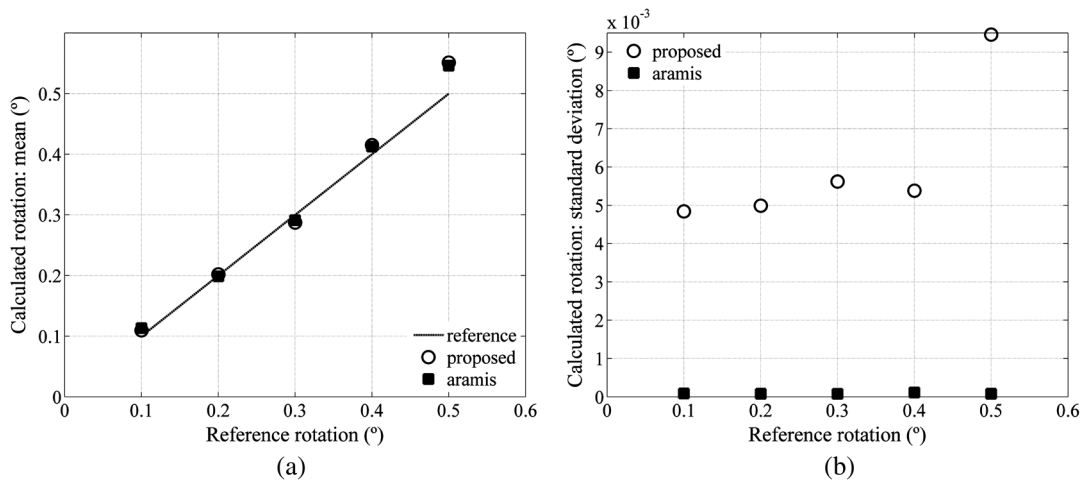


**Fig. 8** In-plane rigid-body rotation test: calculated rotation as a function of reference rotation obtained from proposed (○) and Aramis (■) digital image correlation methods.

displacement fields had a linear variation, as expected in the tensile mechanical test, and were qualitatively equivalent.

The linear strain fields [Eq. (4)] were reconstructed from the measured displacement fields according to the linear strain-displacement relationships. This calculation involves numerical partial differentiation of the displacement field components. Because of the expected homogeneity of the strain fields in this application, polynomial least-squares approximation was used.<sup>27</sup> An order of the polynomial functions equal to 3 was deemed suitable in this case. The engineering strain components were then defined as the mean value calculated over the whole gauge area of the specimen [Fig. 3(c)].

The strains, load, and specimen dimensions were then entered in the closed-form solution of the mechanical tensile test to identify the Young's modulus ( $E$ ) and Poisson's ratio ( $\nu$ ). These results are summarized in Table 2. The mean values of Young's modulus obtained from both the proposed and Aramis DIC methods were in agreement with the reference value of this material. Moreover, a low scatter

(coefficient of variation) was obtained from the measurements of both methods. Similar conclusions were observed for Poisson's ratio. Furthermore, when comparing the elastic properties determined from both methods for each individual sample, a relative difference below or around 1% was systematically obtained. These results validate the proposed method for processing homogeneous strain fields. It is worth noting that although both the proposed and the Aramis methods deliver qualitatively similar results in this application, the proposed method has a higher spatial resolution (Table 1). This can be an advantage in processing more complex and heterogeneous strain fields.

#### 5.4 Mode I Fracture Mechanical Test

The load–displacement curve typically obtained from the SEN-TPB fracture test is shown in Fig. 10(a). The maximum applied load was 72 N, and self-similar crack propagation was reached during a maximum cross-head displacement of 1.2 mm. A sequence of images was recorded during

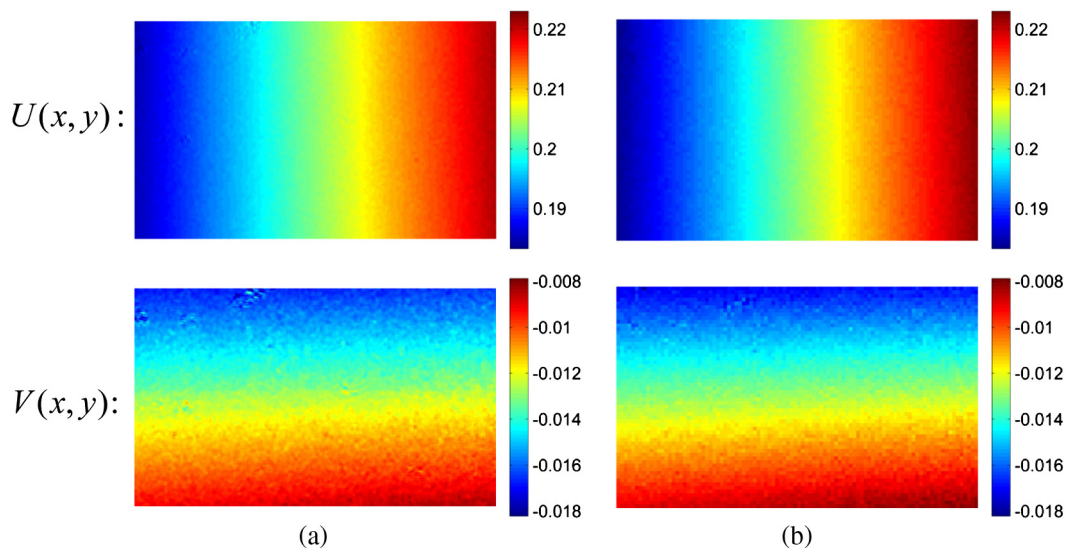


**Fig. 9** Tensile mechanical test:  $U(x,y)$  and  $V(x,y)$  displacement fields obtained from proposed (a) and Aramis (b) digital image correlation methods (unit: mm).

**Table 2** Tensile mechanical test: elastic properties determined from proposed and Aramis digital image correlation methods.

Specimen	$E$ (GPa)			$\nu$		
	Proposed	Aramis	dif. (%) <sup>a</sup>	Proposed	Aramis	dif. (%)
1	2.750	2.756	0.22	0.358	0.360	0.56
2	3.139	3.106	1.06	0.419	0.418	0.24
3	3.050	3.025	0.83	0.380	0.378	0.53
4	3.052	3.027	0.83	0.387	0.393	1.53
Mean	2.998	2.979		0.386	0.387	
C.V. (%) <sup>b</sup>	2.90	2.36		0.49	0.47	

the test, with optical and measuring parameters reported in Table 1. The images were then processed by both the proposed and Aramis DIC methods. The resulting displacement fields were further processed to determine the evolution of crack length and crack opening displacement.

#### 5.4.1 Crack length

The crack length for each recorded image was obtained, processing the respective displacement fields provided by both proposed and Aramis DIC methods according to Eqs. (11) and (12). A threshold value of  $\alpha = 28$  was used in image classification [Eq. (12)]. In Fig. 10(b), the crack length ( $a$ ) is presented as a function of the displacement ( $\delta$ ). The value of  $\delta$  was assumed as cross-head displacement. In the present case, the reference crack lengths were determined by use of the CAD tool directly in the images. From a qualitative point of view, the results determined from proposed and Aramis DIC methods followed the reference ones quite well, especially for low displacement values (<0.5 mm). Nevertheless, when analyzing in more detail the evolution of the crack length during the test, the proposed method gave a better and smoother measurement than Aramis.

The crack length as a function of the applied load was also estimated from the displacement fields [see Fig. 10(c)]. As can be seen, the proposed method reveals that crack propagation takes place before the maximum load is attained. This behavior was also detected by Aramis but less perceptibly. During crack propagation in the post-peak regimen, a more accurate calculation of the crack length was also obtained with the proposed method.

#### 5.4.2 Crack opening displacement

The crack tip opening displacement (CTOD) is defined by the relative distance between two adjacent points chosen across the initial crack length ( $a_0$ ), measured during the crack propagation (Fig. 4). The CTOD value was calculated for each recorded image, processing the displacement fields obtained from the proposed and Aramis methods according to Eq. (13). Also in this case, reference values were measured manually using visual analysis. Two figures were generated: CTOD as a function of displacement ( $\delta$ ) [Fig. 11(a)] and CTOD as a function of applied load ( $P$ ) [Fig. 11(b)].

Both proposed and Aramis methods follow the measured reference CTOD values very closely, although the proposed method delivers a more accurate CTOD measurement. Indeed, the Aramis method tends to overestimate the values of CTOD.

The COD measures the distance separating cracked surfaces at a given distance behind the crack tip (Fig. 4). Also in this case, COD was evaluated from the displacement field components provided by proposed and Aramis methods according to Eq. (13). The field of view of the deformed specimen, corresponding to an applied load of  $P = 57.2$  N and cross-head displacement of  $\delta = 1.15$  mm, is shown in Fig. 12(a). The region of analysis around the crack region and the cross-lines between the pairs of points chosen to calculate COD are shown in Fig. 12(b). The  $U(x, y)$  displacement field over the region of interest measured from the Aramis and proposed DIC methods is displayed in Fig. 12(c) and Fig. 12(d), respectively. To better understand the displacement values, usually obtained across pairs of points and used to calculate COD, a plot was generated in Fig. 12(e), from which the middle position in the  $x$  direction of the plot corresponds to the crack location. It is worth noting that, owing to the pointwise nature of the proposed method, each point in the profile lines has its own displacement value, which is not the case in the results given by Aramis, because of its subset nature. For the sake of comparison and more detailed evaluation, in Figs. 12(f) through 12(h) plots, respectively, the first, fourth, and eighth profiles obtained from the displacement field calculated from both the proposed and the Aramis methods. It is clear from these plots that the pointwise nature of the proposed method enables the accurate calculation of COD. On the other hand, the Aramis method delivers displacement values far from the edge of the crack, which induces a large overestimation of COD.

## 6 Conclusions

In this work, a digital image correlation method combining cross-correlation and spatiotemporal differential techniques was validated through a set of experimental tests. These tests deal with both continuous (rigid-body and tensile tests) and discontinuous (mode I fracture test) displacement fields. The proposed method was systematically compared with the Aramis

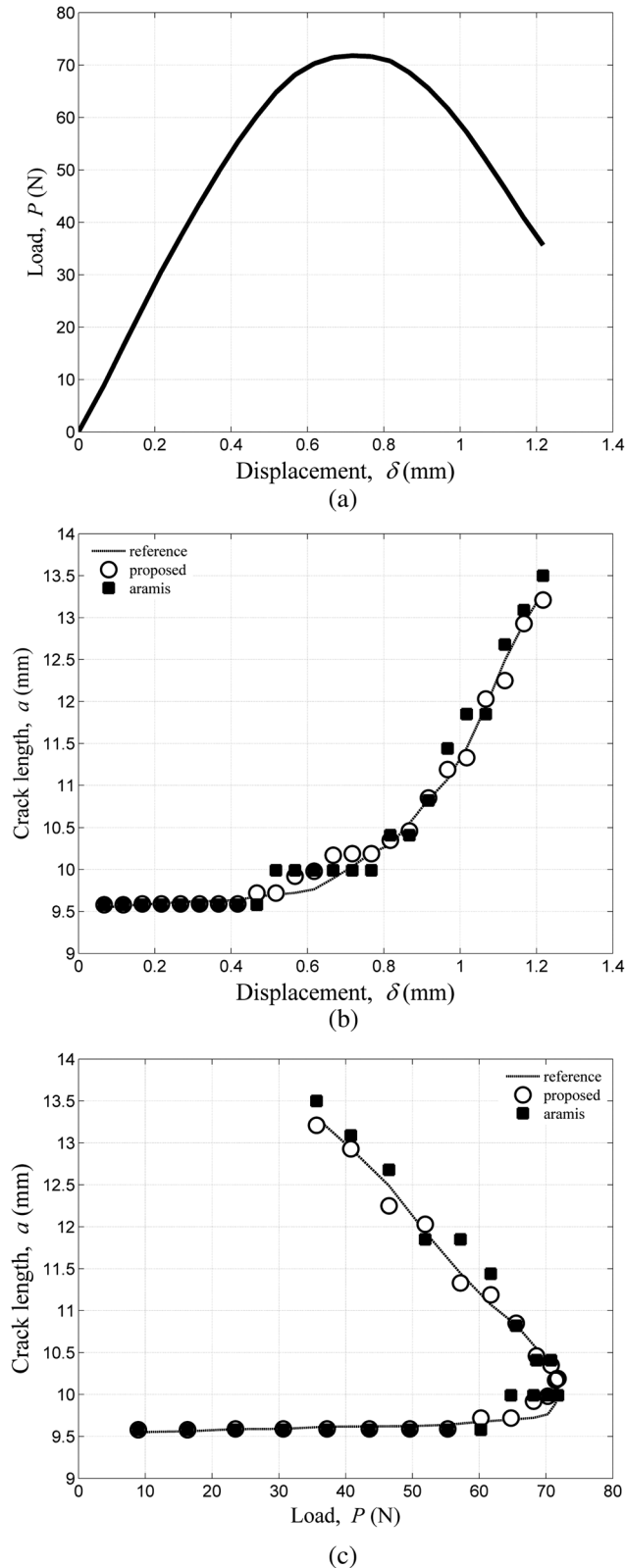


**Fig. 10** Mode I fracture test: (a) load–displacement curve; (b) crack length–displacement curve; (c) crack length–load curve.

DIC-2D commercial code by processing the same set of images. As are most DIC algorithms, Aramis is based on subset image correlation (which size defines the spatial resolution), which is prone to measuring errors when dealing with discontinuous

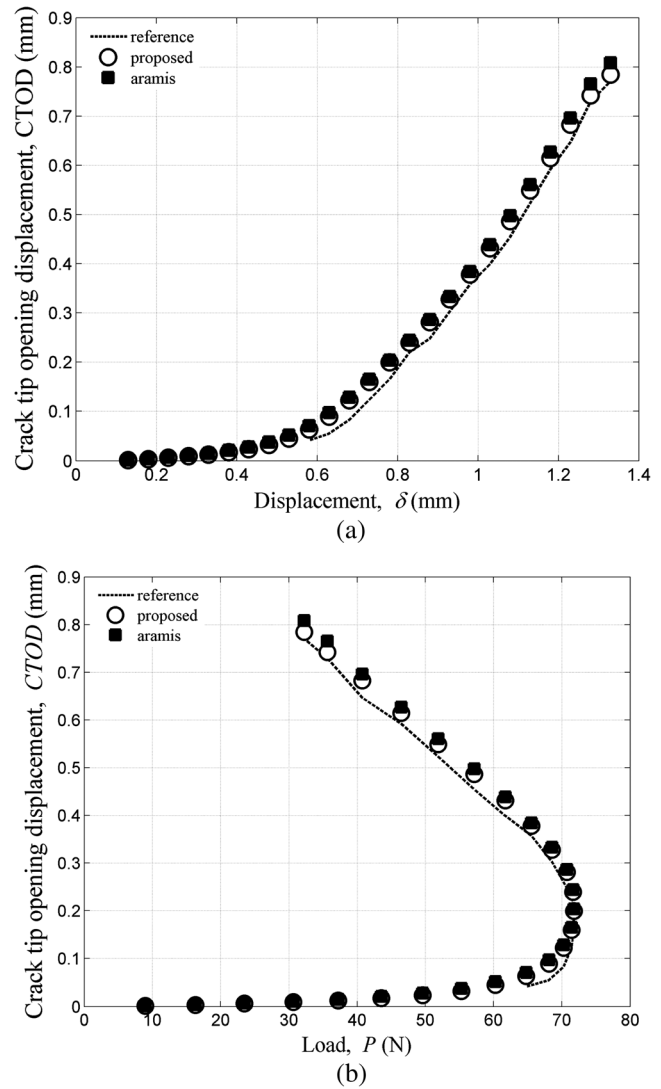


**Fig. 11** Mode I fracture test: (a) crack tip opening displacement–displacement curve; (b) crack tip opening displacement–load curve.

displacement fields and interpolation errors when in the presence of very high strain gradients.

When processing images from rigid-body and tensile mechanical tests, the results obtained from both methods were practically equivalent. In the tensile test, for instance, elastic properties (Young's modulus  $E$  and Poisson's ratio  $\nu$ ) of an epoxy resin were determined from the displacement fields measured by both methods. The values obtained from the two methods represented statistically the same mean and were in good agreement with reference properties of the tested epoxy material. Although both proposed and Aramis methods delivered equivalent results in these cases, the fact that the proposed method has a higher spatial resolution (pointwise) can be an advantage in applications processing more complex and heterogeneous kinematic fields (e.g., heterogeneous tensile tests for multiparameter identification<sup>27</sup>).

In the SEN-TPB mode I fracture test, a better definition of the displacement field around the crack extension was obtained by the proposed method compared with Aramis. For quantitative evaluation, the crack length and the crack

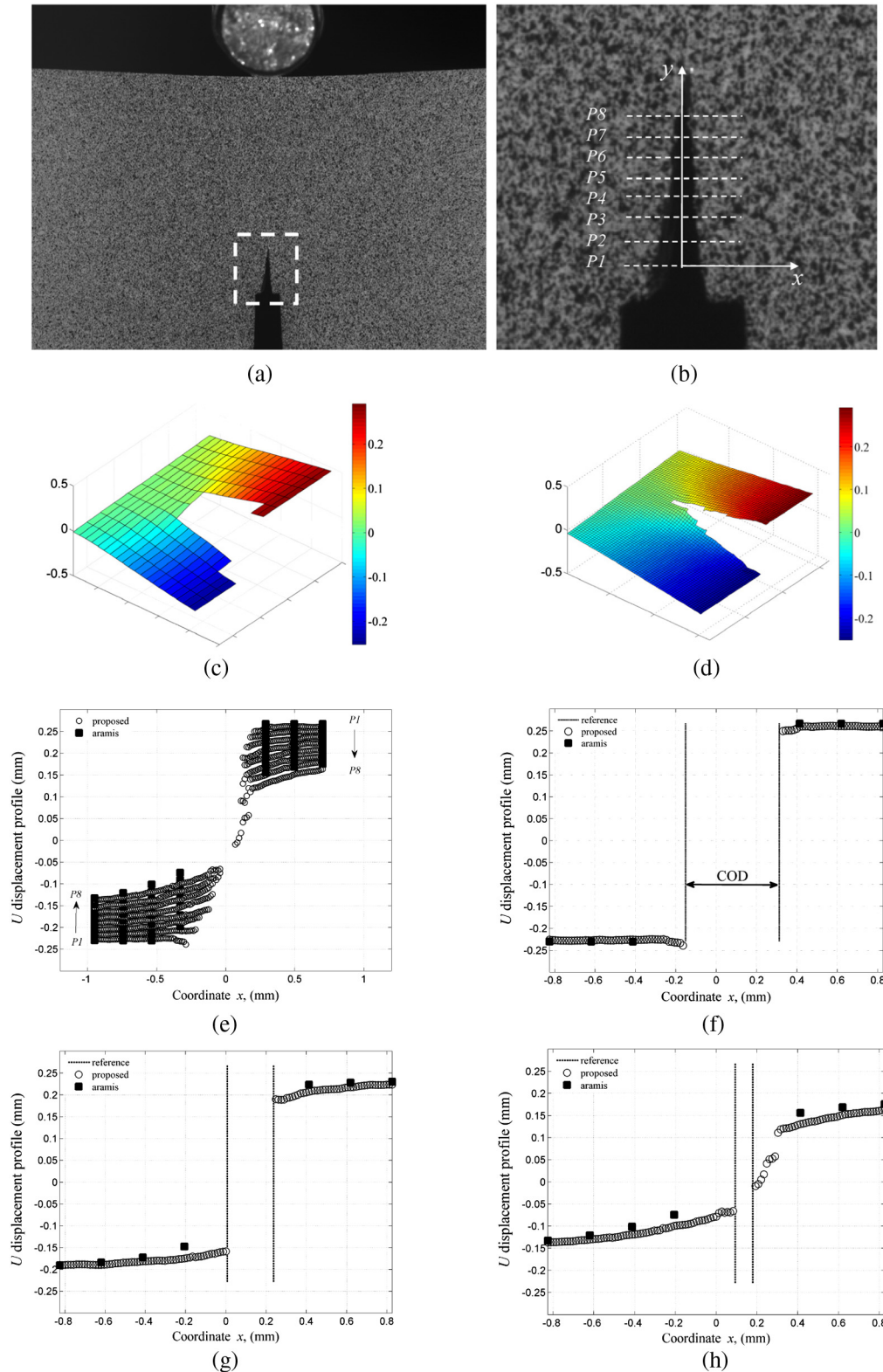


**Fig. 12** Crack opening displacement (COD) ( $F = 57.2 \text{ N}$ ): (a) region of interest around crack extension; (b) line profiles ( $P1, \dots, P8$ ); (c) displacement field from Aramis; (d) displacement field from proposed method; (e) displacement profiles; (f)  $P1$ ; (g)  $P4$ ; (h)  $P8$  (unit: mm).

opening displacement were determined from the displacement fields provided by both methods. The crack length during crack propagation was estimated with more precision by the proposed method. It was also observed that when

evaluating the crack tip opening displacement as the crack starts to propagate, the Aramis method tend to overestimate the values of CTOD compared with proposed method and reference values. For a given crack length during self-similar



propagation, the crack opening displacement was also measured at several distances from the crack tip. In these measurements, it was clear that the pointwise nature of the proposed method enables the accurate calculation of COD in each pair of selected points. On the other hand, owing to its subset correlation algorithm, the Aramis method induces a large overestimation of COD.

In this work, no comparison was established between the proposed method and Aramis in terms of computation time, since the commercial software is a closed solution and we gave more focus to accuracy. As a future work, however, real-time processing will be addressed, since this is an important issue for practical use. Moreover, further test methods can also be addressed to estimate maximum allowed strain and rotation.

### Acknowledgments

The authors thank the Portuguese Foundation for Science and Technology for supporting this work through the research project PTDC/EME-PME/114443/2009 and the *Ciência2008* program.

### References

1. M. Grédiac, "The use of full-field measurement methods in composite material characterisation: interest and limitations," *Compos. Part A-Appl. S.* **35**(7–8), 751–761 (2004).
2. M. Sutton, J.-J. Orteu, and H. Schreier, *Image Correlation for Shape, Motion and Deformation Measurements: Basic Concepts, Theory and Applications*, Springer, New York (2009).
3. B. Pan et al., "Two-dimensional digital image correlation for in-plane displacement and strain measurement: a review," *Meas. Sci. Technol.* **20**, 062001 (2009).
4. M. A. Sutton et al., "The effects of subpixel image restoration on digital correlation error estimates," *Opt. Eng.* **27**(10), 173–175 (1988).
5. P. Bing et al., "Performance of sub-pixel registration algorithms in digital image correlation," *Meas. Sci. Technol.* **17**(6), 1615–1621 (2006).
6. M. Bornert et al., "Assessment of digital image correlation measurement errors: methodology and results," *Exp. Mech.* **49**(3), 353–370 (2009).
7. H. Haddadi and S. Belhabib, "Use of rigid-body motion for the investigation and estimation of the measurement errors related to digital image correlation technique," *Opt. Laser. Eng.* **46**(2), 185–196 (2008).
8. H. Jin and H. Bruck, "Theoretical development for pointwise digital image correlation," *Opt. Eng.* **44**, 067003.1–067003.14 (2005).
9. J. Réthoré, F. Hild, and S. Roux, "Shear-band capturing using a multi-scale extended digital image correlation technique," *Comput. Meth. Appl. Mech. Eng.* **196**(49–52), 5016–5030 (2007).
10. J. Réthoré, F. Hild, and S. Roux, "Extended digital image correlation with crack shape optimization," *Int. J. Numer. Meth. Eng.* **73**(2), 248–272 (2008).
11. N. Moes, J. Dolbow, and T. Belytschko, "A finite element method for crack growth without remeshing," *Int. J. Numer. Meth. Eng.* **46**(7), 131–150 (1999).
12. J. Chen et al., "Deformation measurement across crack using two-step extended digital image correlation method," *Opt. Laser. Eng.* **48**(11), 1126–1131 (2010).
13. J. Poissant and F. Barthelat, "A novel 'subset splitting' procedure for digital image correlation on discontinuous displacement fields," *Exp. Mech.* **50**(3), 353–364 (2010).
14. A. M. R. Sousa et al., "Cross-correlation and differential technique combination to determine displacement fields," *Strain* **47**(s2), 87–98 (2011).
15. A. M. R. Sousa et al., "Processing discontinuous displacement fields by a spatio-temporal derivative technique," *Opt. Laser. Eng.* **49**(12), 1402–1412 (2011).
16. ARAMIS commercial software. GOM, <http://www.gom.com/3d-software/aramis-software.html>.
17. J. L. Barron, D. J. Fleet, and S. S. Beauchemin, "Performance of optical flow techniques," *Int. J. Comput. Vis.* **12**, 43–77 (1994).
18. J. P. Lewis, "Fast Normalized Cross-Correlation," in *Vision Interface Canadian Image Processing and Pattern Recognition Society*, Quebec City, Canada, pp. 120–123 (1995).
19. R. M. Haralick and L. G. Shapiro, *Computer and Robot Vision*, vol. **II**, Addison-Wesley, Reading, MA, pp. 316–317 (1992).
20. B. Lucas and T. Kanade, "An iterative image registration technique with an application to stereo vision," in *Proc. of the 7th International Joint Conf. on Artificial Intelligence – Vol. 2 (IJCAI'81)*, Morgan Kaufmann Publishers Inc., San Francisco, CA, USA, 121–130 (1981).
21. D. Grégoire, "Initiation, propagation, arrêt et redémarrage de fissures sous impact," Ph.D. thesis (LaMCoS-INSA de Lyon, 2008).
22. G. Catalanotti et al., "Measurement of resistance curves in the longitudinal failure of composites using digital image correlation," *Compos. Sci. Technol.* **70**(13), 1986–1993 (2010).
23. T. L. Nguyen et al., "Fracture mechanisms in soft rock: identification and quantification of evolving displacement discontinuities by extended digital image correlation," *Tectonophysics* **503**(1–2), 117–128 (2011).
24. J. Carroll et al., "Investigation of fatigue crack closure using multiscale image correlation experiments," *Eng. Fract. Mech.* **76**(15), 2384–2398 (2009).
25. J. Yates, M. Zanganeh, and Y. Tai, "Quantifying crack tip displacement fields with DIC," *Eng. Fract. Mech.* **77**(11), 2063–2076 (2010).
26. ASTM E399-90, *Standard Test Method for Plane-strain Fracture Toughness of Metallic Materials, Part 3*, American Society for Testing and Materials (1997).
27. J. Xavier et al., "Novel experimental approach for longitudinal-radial stiffness characterisation of clear wood by a single test," *Holzforschung* **61**(5), 573–581 (2007).
28. S. Choi and S. P. Shah, "Measurement of deformations on concrete subjected to compression using image correlation," *Exp. Mech.* **37**(3), 307–313 (1997).

Biographies and photographs of the authors are not available.